ACS NANO Cite This: ACS Nano 2018, 12, 12912−12922 www.acsnano.org
ARTICLE

Capacity Degradation Mechanism and Cycling Stability Enhancement of AlF_3-Coated Nanorod Gradient $Na[Ni_{0.65}Co_{0.08}Mn_{0.27}]O_2$ Cathode for Sodium-Ion Batteries

Ho-Hyun Sun,[†] Jang-Yeon Hwang,[‡] Chong Seung Yoon,[*,§] Adam Heller,[†] and C. Buddie Mullins[*,†,∥]

[†]McKetta Department of Chemical Engineering, The University of Texas at Austin, Austin, Texas 78712-1589, United States
[‡]Department of Energy Engineering, Hanyang University, Seoul 133-791, Republic of Korea
[§]Department of Materials Science and Engineering, Hanyang University, Seoul 133-791, Republic of Korea
[∥]Department of Chemistry, The University of Texas at Austin, Austin, Texas 78712-1224, United States

Supporting Information

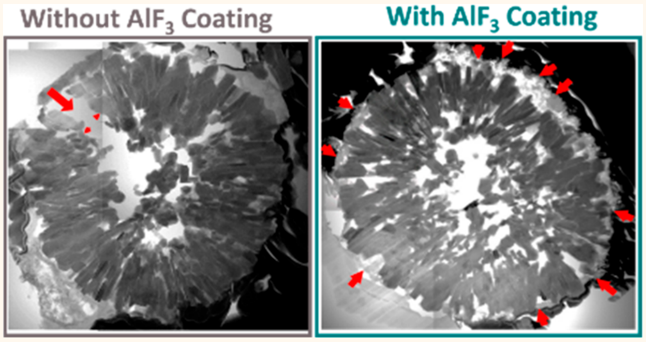

ABSTRACT: O3-type $Na[Ni_xCo_yMn_z]O_2$ materials are attractive cathodes for sodium-ion batteries because of their full cell fabrication practicality, high energy density, and relatively easy technology transfer arising from their similarity to $Li[Ni_xCo_yMn_z]O_2$ materials, yet their performance viability with Ni-rich composition ($x \geq 0.6$) is still doubtful. More importantly, their capacity degradation mechanism remains to be established. In this paper, we introduce an O3-type Ni-rich AlF_3-coated nanorod gradient $Na[Ni_{0.65}Co_{0.08}Mn_{0.27}]O_2$ cathode with enhanced electrochemical performance in both half-cells and full cells. AlF_3-coated nanorod gradient $Na[Ni_{0.65}Co_{0.08}Mn_{0.27}]O_2$ particles were synthesized through a combination of dry ball-mill coating and columnar composition gradient design and deliver a discharge capacity of 168 mAh g^{-1} with 90% capacity retention in half cells (50 cycles) and 132 mAh g^{-1} with 90% capacity retention in full cells (200 cycles) at 75 mA g^{-1} (0.5C, 1.5−4.1 V). Through analysis of the cycled electrodes, the capacity-degradation mechanism was unraveled in O3-type Ni-rich $Na[Ni_xCo_yMn_z]O_2$ from a structural perspective with emphasis on high-resolution transmission electron microscopy, providing valuable information on improving O3-type $Na[Ni_xCo_yMn_z]O_2$ cathode performance.

KEYWORDS: *Ni-rich layered oxide cathode, AlF_3 coating, gradient cathode, Na-ion batteries, O3-type cathode, degradation mechanism, HR-TEM*

With the embracement of electrical energy as a significant energy source, lithium-ion batteries (LIBs) have become prominent as an energy storage device, expanding tremendously from portable electronic devices to larger devices such as vehicles and grid energy storage systems.[1,2] Indeed, the LIB market grew considerably between 1990 and 2013 to a total of \$54 billion (U.S.) and is forecasted to accelerate, especially with the spread of electric vehicles.[3] Despite its tremendous expansion, there has been much concern over the possible exhaustion of lithium sources as it is predicted that lithium shortages could occur due to increased demand.[4,5] This is already reflected in lithium prices doubling over the past few years. Additionally, lithium sources are concentrated in only a few geographical locations, making it vulnerable to price fluctuations. Naturally, alternative energy storage sources have been sought after for some time.

Of the potential candidates, room-temperature sodium-ion batteries (SIBs) have received much attention. Sodium is the sixth most abundant element in the earth's crust, which makes it more cost-effective than lithium,[6] and SIB chemistry is like that of the well-established LIB, which facilitates SIB research.[7] Nonetheless, for SIBs to compete with LIBs, the former need to have comparable electrochemical performance to the latter.

Received: October 29, 2018
Accepted: November 26, 2018
Published: November 26, 2018

DOI: 10.1021/acsnano.8b08266
ACS Nano 2018, 12, 12912−12922

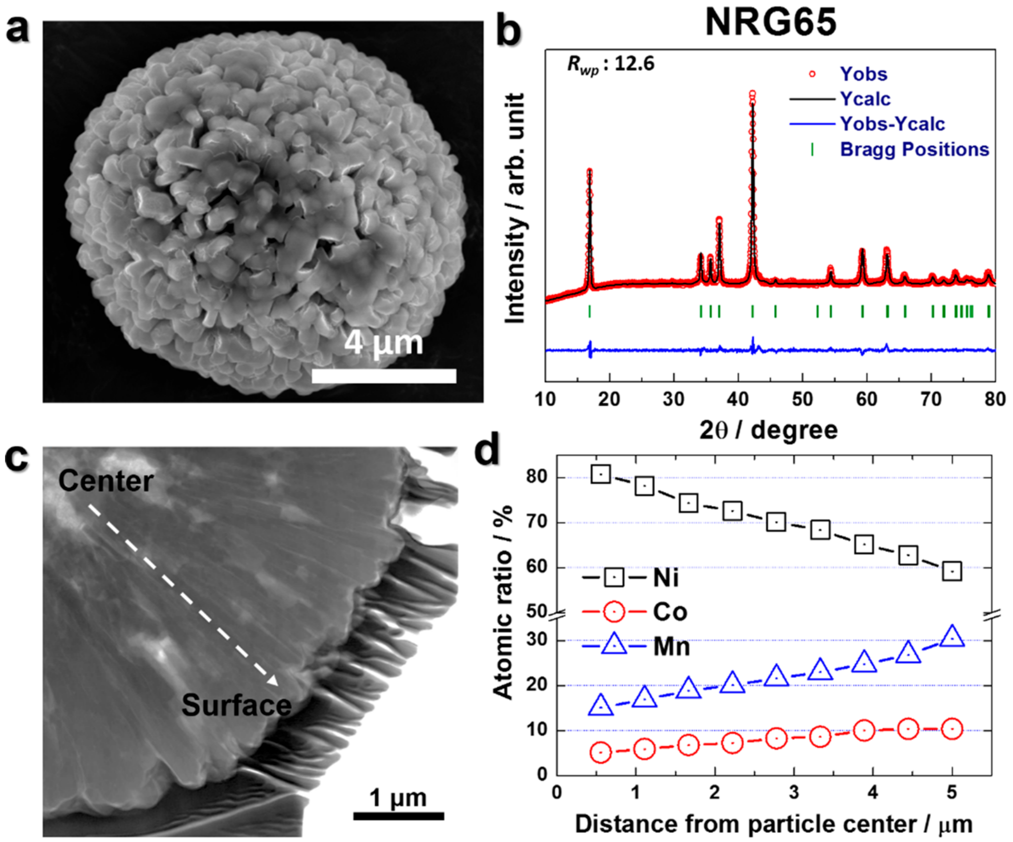

Figure 1. (a) SEM image, (b) Rietveld refined XRD pattern, (c) cross-sectioned TEM image, and (d) EPMA data of as-synthesized nanorod gradient $Na[Ni_{0.65}Co_{0.08}Mn_{0.27}]O_2$.

To achieve this, various SIB cathodes have been studied, including polyanion structures,[8,9] organic compounds,[10] and P2-type[11−15] and O3-type layered oxides.[16−23] Among the various candidate materials, the layered oxide compounds appear to be most attractive as a promising cathode for SIBs because of their high gravimetric energy density and cycling stability. Recently, P2-type layered oxide materials (Na_xMO_2, $x \approx 0.7$) have garnered much attention due to their high reversible capacities and fascinating crystal structure. But the initial sodium deficiency results in an atypical coulombic efficiency (≥100%) during the initial formation cycle and hampers full cell fabrication, ultimately making them impractical.[24] On the other hand, O3-type layered oxides $NaMO_2$ (M: transition metals) possess the same crystal structure and chemistry as the prominent $LiCoO_2$[25] and can still be fabricated into practical full cells. In particular, spherical co-precipitation synthesized layered O3-type $Na[Ni_xCo_yMn_{1-y}]O_2$ (Na-NCM) has been of interest because of its high tap density[15] and basis in the prominent layered $Li[Ni_xCo_yMn_{1-x-y}]O_2$ (Li-NCM) chemistry, making Na-NCM technology transfer relatively easy.

On the basis of previous works, increasing the Ni content in Na-NCM has shown to be crucial in fundamentally increasing its energy density in a similar way to Li-NCM chemistry.[20] This is a double-edged sword though as Na-NCM also suffers from accelerated capacity fade with increasing Ni content due to the high reactivity of Ni^{4+} with electrolyte, but with heightened intensity compared to Li-NCM and also at Ni-rich conditions of over 60% Ni. Additionally, above 4.0 V, O3-type Na-NCM experiences unwanted electrolyte side reactions and structural instabilities, further contributing to capacity fade (additional comments on the voltage window are contained in the Methods).[20] In LIBs, a myriad of strategies have been explored to alleviate the detrimental effect of surface degradation on reversible capacity.[26−29] Similarly, coating with compounds such as $NaPO_3$, MgO, TiO_2, ZrO_2, and Al_2O_3[30−36] has been a successful strategy in SIBs. Unfortunately, there is a dearth of publications regarding SIB-layered cathode surface modifications compared to LIB cathode surface modifications, even though cathode surface modification is critical to SIB battery performance. Additionally, many of the processes used in LIB cathodes are not suitable for SIB cathodes as they employ solvents or require an additional calcination treatment which may expose the cathode to moisture or thermal stress.[7,36]

To bypass potentially irreversible damage to the cathode and resolve the reactivity of Ni-rich Na-NCMs, Sun *et al.* developed a dry ball-mill coating process using Al_2O_3, which reacts with electrolyte to form an AlF_3 protective layer, to successfully suppress surface degradation.[36] Another successful approach has been the design of a radially nanocolumnar structured cathode with a transition-metal concentration gradient to achieve minimized metal redox reactions on the surface for chemical stability.[37,38] Despite such successes, Ni-rich Na-NCM is still relatively unexplored in contrast to its lithium counterpart, and a clear understanding of the capacity fading mechanism in Ni-rich Na-NCM is absent at the present. As such, for the development of a realistic SIB, both a high-performance Ni-rich Na-NCM cathode and understanding of the cathode degradation mechanism need to be realized.

In this study, a combination of radially nanocolumnar composition gradient design and dry ball-mill coating was used

DOI: 10.1021/acsnano.8b08266
ACS Nano 2018, 12, 12912−12922

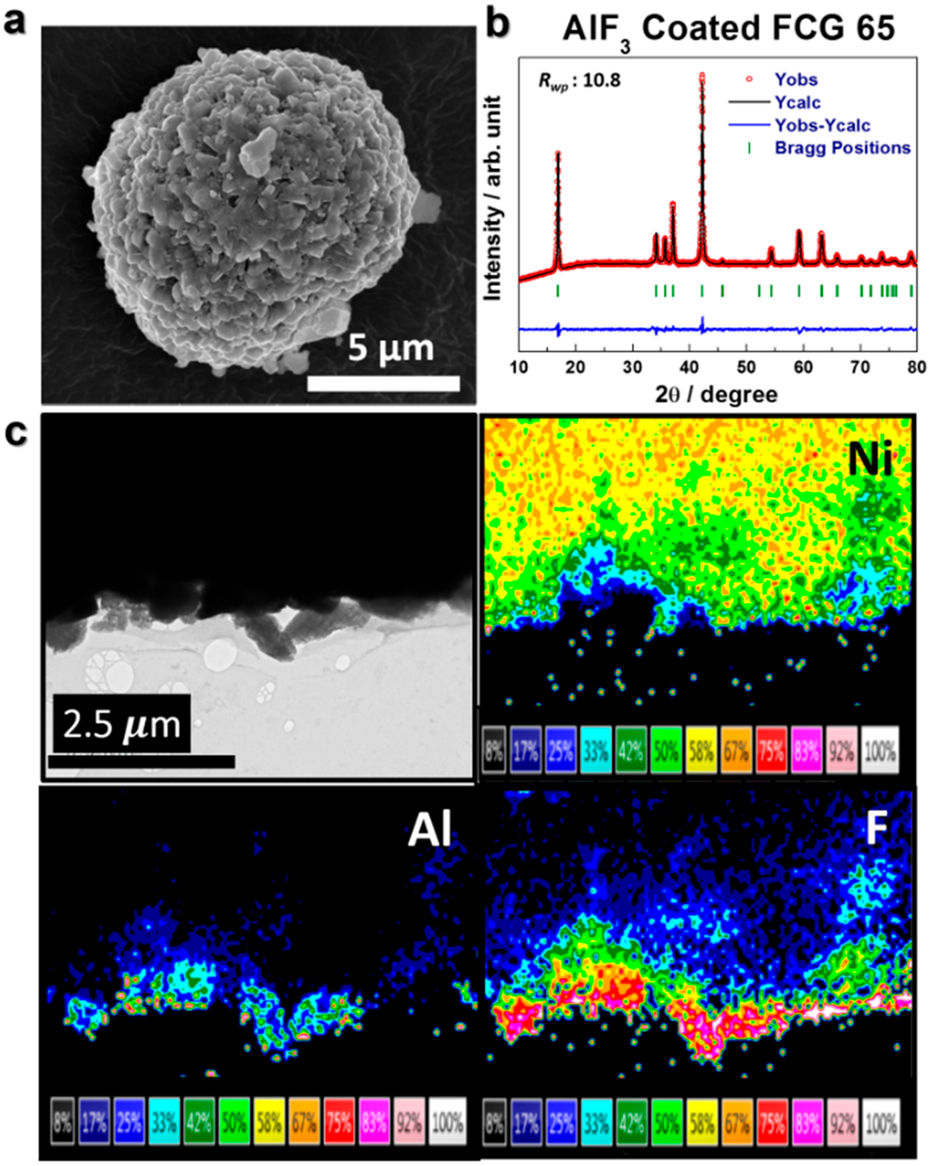

Figure 2. AlF$_3$-coated NRG65 (a) particle SEM image, (b) Rietveld refined XRD pattern, and (c) TEM−EDX quantitative elemental mapping of Ni, Al, and F concentrations near particle surface. Note that the colors indicate the concentration intensity of Ni, Al, and F as indicated by the concentration % shown at the bottom of each images.

for achieving a synergistically high capacity and stable cycling performance for a Ni-rich Na[Ni$_{0.65}$Co$_{0.08}$Mn$_{0.27}$]O$_2$ cathode. The nanorod gradient Na[Ni$_{0.65}$Co$_{0.08}$Mn$_{0.27}$]O$_2$ (NRG65) particle was comprised of a Ni-rich core for high capacity and Mn-rich surface for cycling stability and presents superior electrochemical performance compared to constant concentration Na[Ni$_{0.65}$Co$_{0.08}$Mn$_{0.27}$]O$_2$. To further enhance cycling performance, surface stabilization of the NRG65 was achieved *via* a dry ball-mill coating process using aluminum fluoride (AlF$_3$) as the coating medium. This approach improves upon the previous Al$_2$O$_3$ coating[36] as it circumvents electrolyte side reaction/decomposition with Al$_2$O$_3$ by applying the final AlF$_3$ product as a protection layer in a simple one-step process to delay active material dissolution. Additionally, AlF$_3$ is more stable than Al$_2$O$_3$ as it has a lower Gibbs free energy of formation[39] and is stable up to 4.5 V, and fluorides are also considered to be more resistant to moisture in ambient air than oxides.[40] It is also a tried-and-true coating material in LIB cathodes.[29,39,41,42] As a result, AlF$_3$-coated NRG65 exhibits a high specific capacity and stable cycling performance in both half cells and full cells. More importantly, through a systematic analysis of the cycled cathodes, this work highlights the capacity degradation mechanism of O3-type layered Ni-rich Na[Ni$_x$Co$_y$Mn$_z$]O$_2$ from electrochemical and structural perspectives, with a focus on high-resolution TEM analysis. In the process, we hope to provide a step forward toward the future development of realistic high energy density SIBs.

RESULTS AND DISCUSSION

A scanning electron microscopy (SEM) image of the [Ni$_{0.65}$Co$_{0.08}$Mn$_{0.27}$](OH)$_2$ precursor is shown in Figure S1a. Here, we refer to "secondary particles" as the individual spherical cathode particles which have a uniform size distribution of 8−10 µm in diameter (tap density of ~2.00 g cc^{-1}) and are composed of smaller needle-like nanoscale structures in a radial configuration which we refer to as "primary particles". Thermally sodiated bare (no AlF$_3$ coating) nanorod gradient Na[Ni$_{0.65}$Co$_{0.08}$Mn$_{0.27}$]O$_2$ (NRG65) particles

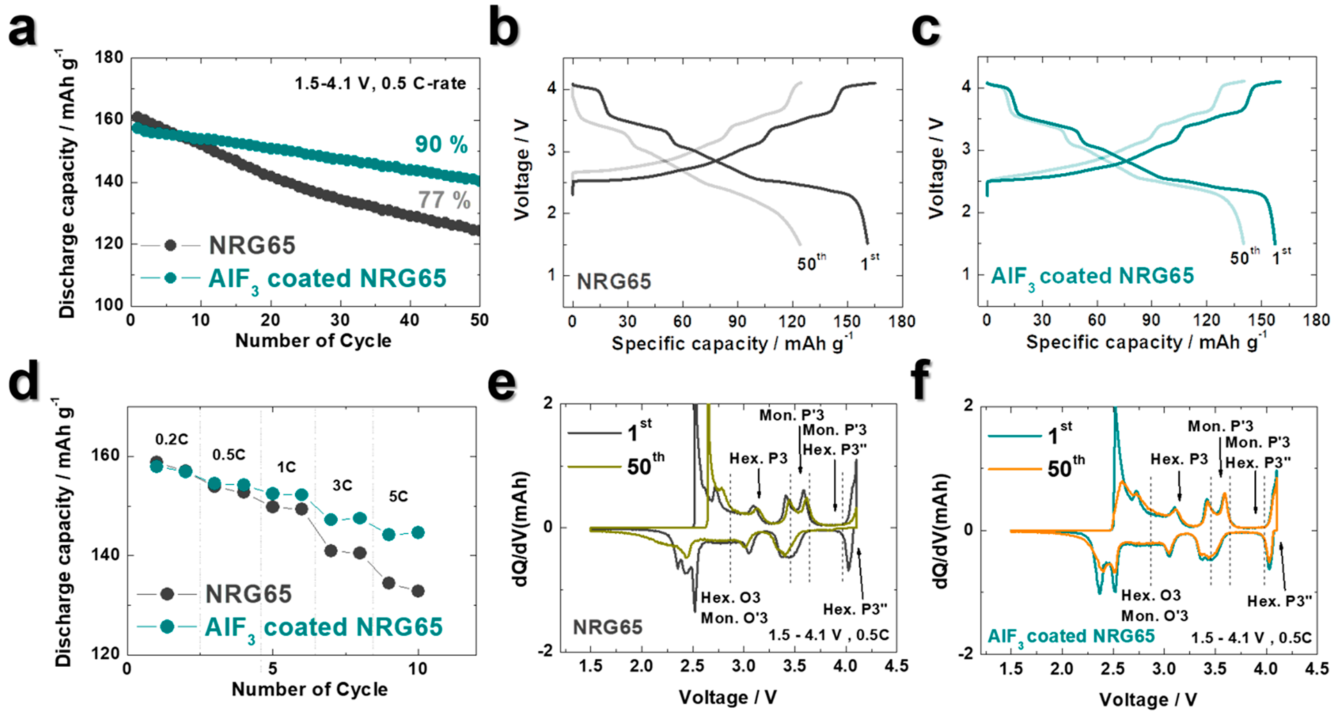

Figure 3. Comparison of electrochemical performances between bare NRG65 and AlF_3−NRG65 in half-cell: (a) cycling performance and corresponding charge−discharge curves at 1st and 50th cycles of (b) bare NRG65 and (c) AlF_3-coated NRG65. (d) Rate capability. dQ dV^{-1} profiles of 1st and 50th cycles of (e) bare NRG65 and (f) AlF_3-coated NRG65.

retain their uniform spherical morphology, but the primary particles became bulkier due to sintering (Figure 1a and Figure S1b). The X-ray diffraction (XRD) pattern and Rietveld refinement of the oxide (Figure 1b) reveaed that the sodiated cathodes had a well-ordered O3-phase with a $R\bar{3}m$ space group and lattice parameters of a = 2.945 (1) Å and c = 15.756 (2) Å (R_{wp} = 12.6).[16,43,44] The proposed NRG cathode design was based on the physiochemical feature shown previously by gradient materials:[45,46] The Ni-rich center delivers a high discharge capacity and the Mn-rich surface minimizes surface reactivity, while the linear transition-metal concentration variation throughout engenders columnar nanorods to minimize anisotropic volume changes from composition differences. An electron probe microanalyzer (EPMA) (Figure 1d) was used to study the transition-metal compositions of the as-synthesized NRG65 to verify the presence of a concentration gradient from particle center to surface to ensure successful nanorod gradient synthesis. The $Na[Ni_{0.65}Co_{0.08}Mn_{0.27}]O_2$ had transition-metal concentrations of 81 atom % Ni, 5 atom % Co, and 14 atom % Mn in the core and 59 atom % Ni, 10 atom % Co, and 31 atom % Mn on the surface and composition gradients in between.[47] Finally, a TEM image of a cross-sectioned nanorod gradient oxide particle (Figure 1c) reveals that NRG65 was composed of compactly packed nanorods that spanned from the center to the surface, confirming that NRG65 was synthesized successfully.[38] Overall (volume averaged) transition-metal compositions were determined by inductively coupled plasma atomic emission spectroscopy (ICP-AES) as seen in Table S1.

AlF_3-coated nanorod gradient $Na[Ni_{0.65}Co_{0.08}Mn_{0.27}]O_2$ (AlF_3−NRG65) particles were obtained *via* dry ball-mill coating with AlF_3 nanoparticles as shown in Figure 2a. As the figure shows, the AlF_3 coating did not alter the spherical morphology of the original particle, but the coating filled the pores that are present in bare NRG65 and roughened the particle surface. The XRD pattern of the coated oxide (Figure 2b) showed almost the same lattice parameters as bare particle (a = 2.943 (1) Å and c = 15.772 (2) Å R_{wp} = 10.8).[16,43,44] SEM-EDX of the AlF_3−NRG65 particle cross-section as displayed in Figure S2 shows that Al signals were detected from the particle surface and that the coating was nonuniform with thicknesses varying from 50 nm thin to 300 nm thick. It should be noted that while a thick coating layer is not beneficial for some aspects regarding cathode performance, due to sodium-based oxide layers being so reactive with electrolyte and moisture, a 200 nm thick coating layer still efficaciously protects the O3-type layered cathode from electrolyte attack and other coating works also have thicknesses of ∼100 nm and show significantly improved performance.[36] Quantitative elemental mapping by energy-dispersive X-ray spectroscopy (EDX) (Figure 2c) also revealed that the outer surface signals consisted of Al and F in an approximately 1:3 ratio, like the molar ratio of AlF_3. Additionally, Ni signals are stronger in the bulk than the surface, providing further evidence of the compositional gradient. As such, it was affirmed that the desired concentration gradient of Ni, Co, and Mn throughout the entire cathode particle was achieved with a nickel-rich core for high capacity and a manganese-rich surface for cycling stability in a columnar nanorod structure[38] and that the coating was indeed AlF_3 for surface protection from acidic species such as HF.

The effect of the synthesized nanorod gradient $Na[Ni_{0.65}Co_{0.08}Mn_{0.27}]O_2$ particle is evident in its electrochemical performance (Figure 3a−d). For comparison, we synthesized a constant (uniform) concentration $Na[Ni_{0.65}Co_{0.08}Mn_{0.27}]O_2$ (CC65) particle, as shown in Figure S3a, and compared the electrochemical performances. When cycled from 1.5 to 4.1 V

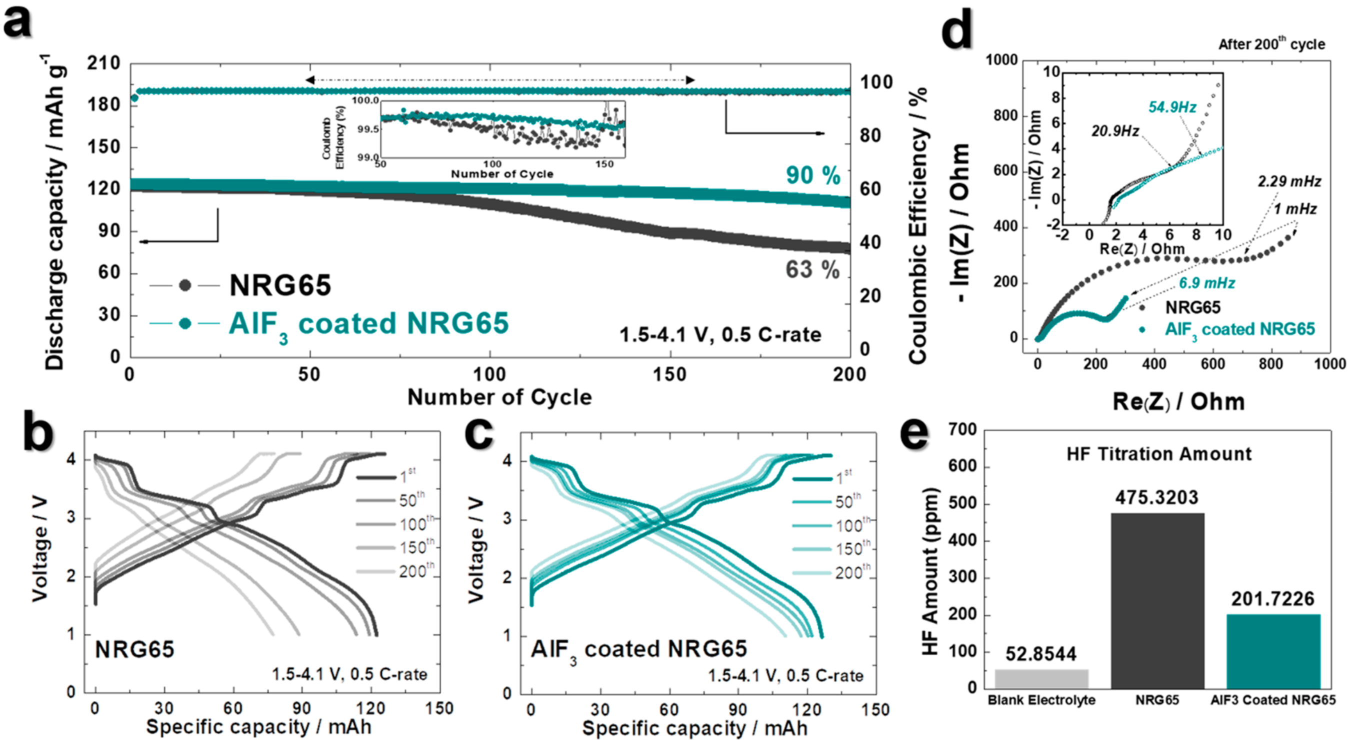

Figure 4. Comparison of electrochemical performances between bare NRG65 and AlF_3−NRG65 in full cells: (a) cycling performance and efficiencies and corresponding charge−discharge curves from the 1st to 200th cycle at a 0.5 C rate of (b) bare NRG65 and (c) AlF_3−NRG65. (d) Electrochemical impedance spectroscopy results at the 200th cycle at 0.5 C rate. (e) HF titration test result.

at 0.5 C (Figure S3b−d), the bare NRG65 cell exhibited much better electrochemical performance than that of CC65 of identical average chemical composition; NRG65 had a discharge capacity of 168 mAh g^{-1} and capacity retention of 77% while CC65 had a discharge capacity of 161 mAh g^{-1} and capacity retention of 64% with the former outperforming the latter also in rate capability performance, especially at high C-rates above 1C.[37,38] It is worth noting that the CC65 charging curve dragged on above 4.0 V and its charging capacity was much higher than discharging capacity, pointing to undesired side-reactions caused by unstable Ni^{4+} on the surface, which is less prevalent in NRG65. Note that such reactions result in electrolyte decomposition and subsequent evolution of gaseous products such as CO_2. The superior performance of the nanorod gradient cathode material is derived from its compositional variation, which exploits the Ni^{3+}/Ni^{4+} redox reaction having a lower energy level than Ni^{2+}/Ni^{3+}, as suggested by Delmas *et al.*[48] In the nanorod gradient oxide, the Ni-rich center is dominated by Ni^{3+}/Ni^{4+} redox reactions, while the Mn-rich surface is dominated by Ni^{2+}/Ni^{3+} redox reactions, explaining why the NRG65 material simultaneously yields more capacity while achieving higher cycling stability compared to CC65 of identical average composition. Despite such merits, the capacity fade of the NRG65 material occurs too rapidly to be considered as a practical SIB cathode and needs improvement.

In order to further improve the electrochemical performance, a coating of AlF_3 was applied to the NRG65 surface. With a layer of AlF_3, the AlF_3−NRG65 cell delivered a 161 mAh g^{-1} first-discharge capacity but retained 90% of its initial discharge capacity (after 50 cycles), which was significantly higher than the bare NRG65 retention rate (Figure 3a). Moreover, both cells showed similar first charge−discharge voltage profiles, but the AlF_3−NRG65 cell better maintained a charge−discharge profile similar to its first as seen in Figure 3b,c; this is reflected in the 1st and 50th cycle dQ dV^{-1} curves of the two cells (Figure 3e,f), which exhibited transition redox peaks correlating to distinct phase transitions where AlF_3−NRG65 better maintained its redox peaks. In particular, the peak from 4.0−4.1 V, which indicates a Ni redox reaction,[15,20] disappeared by the 50th cycle in NRG65, whereas this peak remained unchanged in AlF_3−NRG65 due to the coating layer preventing surface degradation. Note that the arrows indicate the structural phases that are present at the peaks and dash lines indicate the borders in between. Likewise, after-cycled XRD patterns of bare NRG65 and AlF_3−NRG65 demonstrated that the AlF_3-treated material better preserved its structure as the former lost many of its original XRD peaks between 30−40° and possessed a broadened $(003)_{hex}$ peak which also shifted and merged with the monoclinic O3 (001) peak (Figure S4). On the other hand, even though the after-cycled AlF_3−NRG65 electrode showed a monoclinic O3 (001) peak corresponding to 10% Na extraction,[22] it retained its original peaks with minimized peak broadening or weakening. At an elevated temperature of 55 °C (Figure S5), both bare and AlF_3-coated NRG65 showed increased discharge capacities of 163 mAh g^{-1} and 166 mAh g^{-1}, respectively, with the latter showing better capacity retention at the end of the 30th cycle. Not surprisingly, the AlF_3−NRG65 exhibited outstanding rate capability at the faster rates of 3C (450 mA g^{-1}) and 5C (750 mA g^{-1}), where it delivered high discharge capacities of 147 mAh g^{-1} (92.1% of 0.2C) and 145 mAh g^{-1} (90.2% of 0.2C), respectively. It should be noted that NRG65 still exhibited better rate capabilities than the CC (constant composition) materials reported previously[20] due to the elongated nanorods

DOI: 10.1021/acsnano.8b08266
ACS Nano 2018, 12, 12912−12922

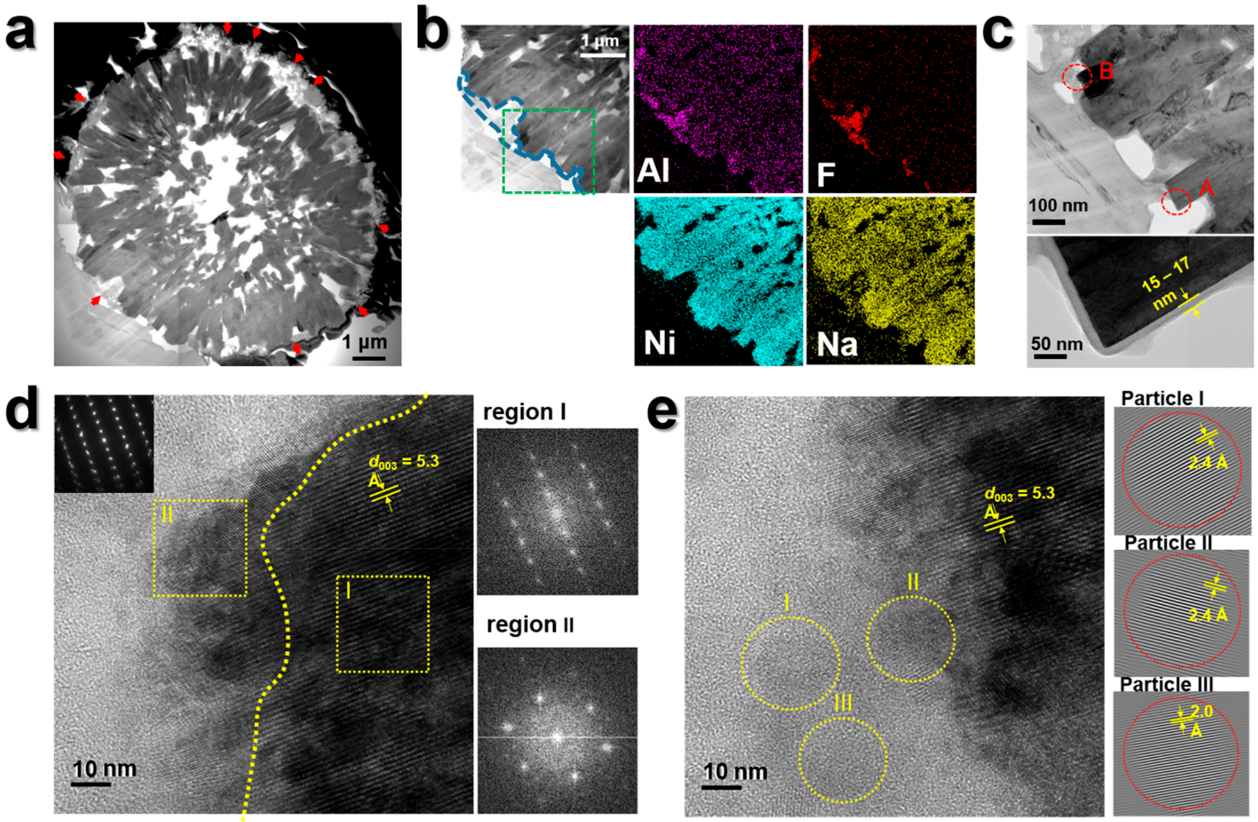

Figure 5. (a) Bright-field scanning TEM cross-sectional image of the cycled AlF_3−NRG65 cathode particle after 200 cycles (red arrows indicate the AlF_3 coating remaining intact after cycling), (b) EDS elemental mapping of the cycled AlF_3−NRG65 cathode particle, (c) bright-field TEM image of the cycled AlF_3−NRG65 cathode marked by the green dashed box in (b) (the figure below shows the magnified image of the area marked A), (d) high-resolution TEM image of the region marked B in (c) and Fourier transform images of the regions I and II, and (e) high-resolution TEM image showing the crystalline secondary phases observed within the AlF_3 coating layer and Fourier-filtered images of the marked secondary phases.

providing for more rapid Na^+ transport through their entire volume.

The impact of the AlF_3 surface coating treatment on the nanorod gradient $Na[Ni_{0.65}Co_{0.08}Mn_{0.27}]O_2$ particles can be seen more clearly in practical pouch-type full cells (cathodes: bare NRG65 and AlF_3−NRG65, anode: hard carbon) as seen in Figure 4. The bare NRG65 and AlF_3-coated NRG65 full cells both delivered similar first-cycle discharge capacities of 130 and 132 mAh g^{-1}. Nevertheless, due to the AlF_3 coating layer shielding the cathode from irreversible damage, the capacity retention of the AlF_3−NRG65 was 90% at 0.5C after 200 cycles and possessed a stable coulombic efficiency throughout cycling. In contrast, the bare NRG65 full cell cycle stability and coulombic efficiency started to falter after the 50th cycle (as seen in the magnified inset of Figure 4a showing the coulombic efficiency) due to exposed active materials reacting with electrolyte and deteriorating to a capacity retention of 63%. Correspondingly, the cell with the AlF_3 surface treated material better retained its charge−discharge character compared to the cell with untreated material which suffered from capacity and voltage fade with progressive cycles (Figure 4c,d). Nyquist plots of the electrochemical impedance (Figure 4b) corroborate said cell performance as by the 200th cycle the charge-transfer (R_{ct}) resistance of the surface modified cell was 225.0 Ω, significantly lower than the 753.8 Ω of the bare cell. Additionally, an HF titration test revealed that the amount of HF (ppm) detected in the bare NRG65 electrode was more than twice that of the AlF_3−NRG65 electrode.

To investigate the promising electrochemical performance of the AlF_3−NRG65 particles, cross-sectional TEM samples from the cycled electrodes of the full cells were fabricated using a focused ion beam. The dark-field scanning TEM image of the cycled AlF_3−NRG65 particle in Figure 5a shows that the AlF_3 coating layer (marked by red arrows) remained intact around the periphery of the secondary particle. The AlF_3 coating was as thick as 1 μm at some places even after 200 cycles. Judging by the before-cycling coating thickness estimated from the EDS mapping in Figure 2, the AlF_3 coating was hardly damaged and incurred no significant materials loss during cycling. The EDS mapping of Al, F, Ni, and Na in Figure 5b confirms the presence of the AlF_3 coating layer (marked by blue dashed lines) filling in the valley between the two protruding primary particles when the Ni and Al (or F) elemental maps are compared. In addition to Al, a strong Na signal was detected in the coating layer, suggesting that Na reacted with the AlF_3 to form new compounds in the coating that improved the cycling stability. Figure 5c shows a bright-field TEM image of the surface region of the cycled AlF_3−NRG65 cathode particle marked by a green dashed box of Figure 5b, and the accompanying magnified image of area “A” indicates that the even the surfaces that appeared uncoated were encapsulated by a thin layer (~10 nm in thickness) such that the AlF_3 coating extended all around the secondary particle and effectively protected the cathode surface. A high-

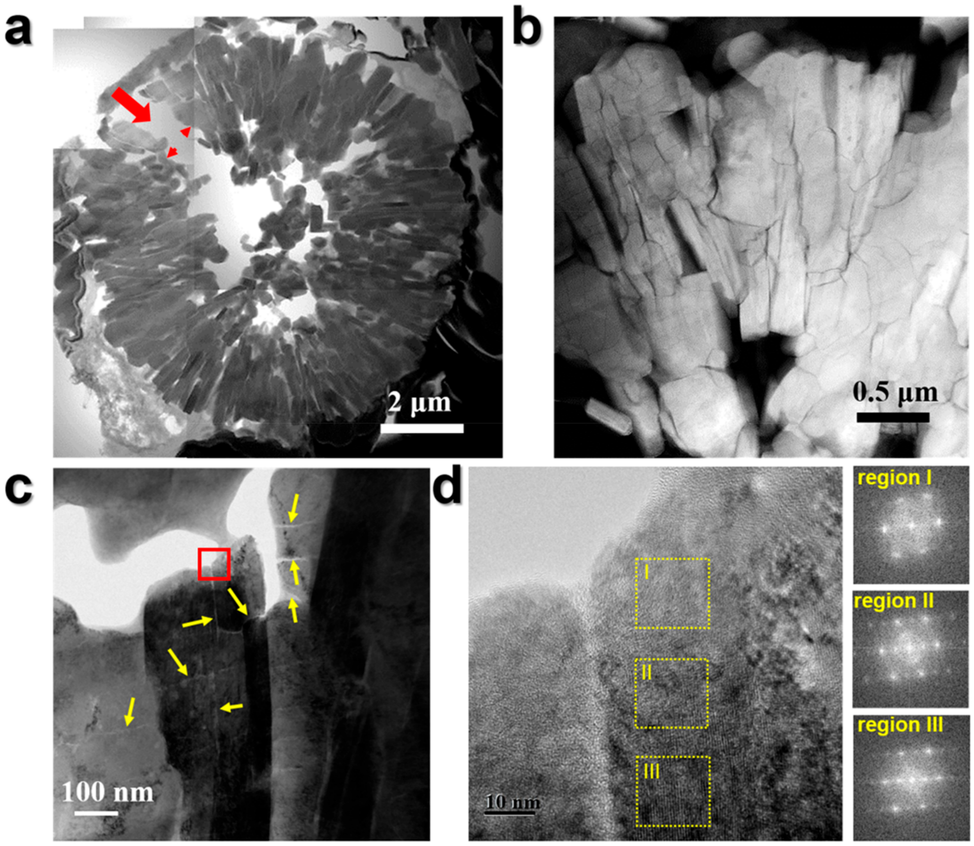

Figure 6. (a) Bright-field scanning TEM cross-sectional image of the cycled bare NRG65 cathode particle after 200 cycles (red arrows indicate a major crack in the secondary particle that allows infiltration of the electrolyte into the particle interior), (b) dark-field scanning TEM image of the cycled bare NRG65 cathode, showing numerous intraparticle cracks, (c) bright-field TEM image of the cycled bare NRG65cathode with the yellow arrows indicating the intraparticle microcracks, and (d) high-resolution TEM image of the red box marked region in (c) and Fourier transform images of regions I, II, and II demonstrating the extensive transition to the rocksalt structure at the surface of the cycled bare NRG65cathode.

resolution TEM image along the 100 zone axis of a primary particle (Figure 5d) of the area marked by B in Figure 5c affirmed retention of the original structure in the particle interior, which was capped by a thin layer of NiO-like rock salt structure. The thickness of the surface rock salt layer was limited to 10−30 nm. Fourier-transform images of the regions I and II in the dotted red boxes clearly distinguishes the two distinct structures. The Fourier transform of the particle interior reproduced the SAED pattern shown in the inset of Figure 5d, whereas some of the diffraction spots became extinct in the Fourier transform of the surface region due to the disordering of the cations in the rock salt structure. Despite a thin layer of partially collapsed structure at the very edge, the layered structure just inside the particle periphery and further in the interior is preserved, which explains the improved cycling stability and the superior rate of the AlF_3−NRG65 cathode. In addition to the surface rock salt layer, isolated secondary crystalline phases were observed near the vicinity of the cycled cathode surface (Figure 5e). The crystalline phases in the surrounding AlF3 coating layer are marked in Figure 5e. The accompanying Fourier filtered images of the marked regions verify the presence of a crystalline phase, and the estimated distances between the lattice fringes were 2.0 and 2.4 Å. Surveying the XRD database, possible compounds containing any combination of Na, Al, F, and O (and with strong peaks at 2.0 Å and/or 2.4 Å) are NaF ($Fm\bar{3}m$, a = 4.62 Å)[49] and $Na_5Al_3F_{14}$ ($P4/mnc$, a = 7.014 Å and c = 10.402 Å).[50] Since the EDS mapping revealed a significant presence of Na in the cycled coating layer, it is likely that AlF_3 reacted with Na to form such compounds. These compounds near the cathode surface may have stabilized the interface chemistry (protection from HF attack and prevention of Ni^{4+} oxidation) and lowered the interface charge transfer resistance by assisting Na^+ conductivity in a similar way that lithium containing compounds reduce ion resistance to improve electrochemical performance.[40,51,52]

As shown in Figure 6a, the cycled bare NRG65 cathode particle contained a large crack that nearly fractured the secondary particle due to stress from repeated Na intercalation/deintercalation and the opening created by the crack allowed the infiltration of electrolyte into the particle interior, accelerating the electrolyte attack of the exposed interior surfaces. The dark-field scanning TEM image in Figure 6b shows that individual primary particles in the cycled bare NRG65 cathode suffered from numerous intraparticle cracks. Hence, without the AlF_3 coating, the bare NRG65 cathode particles lost their mechanical integrity from the intergranular fracture as well as from the structural undermining of the primary particles themselves. The bright-field TEM image in Figure 6c confirms the intraparticle fracture by revealing a network of numerous hairline microcracks nucleated within a primary particle as pointed out by yellow arrows. In addition to the observed hairline microcracks, the high-resolution TEM of the surface area of the primary particle in Figure 6d indicates

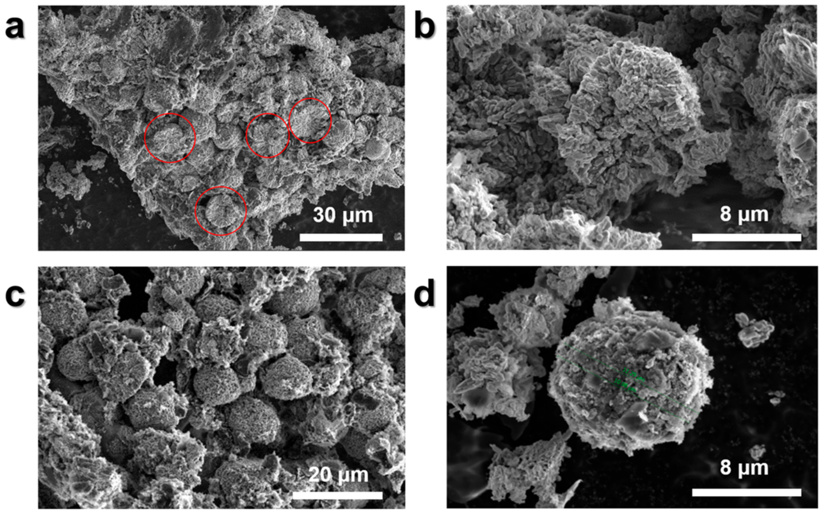

Figure 7. Post-mortem analysis: SEM images of the cycled (a, b) BARE NRG65 (red circles point out pulverized particles) and (c, d) AlF_3−NRG65 electrodes collected from the pouch-type full cells after 200 cycles.

that the phase transition to the rocksalt structure arising from the cation intermixing persisted well into the particle interior. The Fourier transform of region III which is approximately 100 nm away from the particle surface still contains strong diffraction peaks corresponding to the rocksalt structure on the background pattern of the layered structure. This contrasts sharply with the surface structure of the cycled AlF_3−NRG65 cathode in which the damaged rocksalt layer was confined to ∼20 nm. The thick damaged surface layer and the observed loss of the mechanical integrity well explains the rapid capacity fade of the bare cathode and immensely large value for R_{ct} of the bare full cell electrode. In this regard, the O3-type Ni-rich $NaNi_xCo_yMn_zO_2$ capacity fading mechanism is very much like that of the LIB layered $LiNi_xCo_yMn_zO_2$ in which the cathode structure breaks down from mechanical stress imposed by numerous phase transitions with the surface degrading from electrolyte side-reactions followed by electrolyte penetration into the bulk and accelerated capacity fade.[47,53,54] However, SIB $NaNi_xCo_yMn_zO_2$ undergoes more phase transitions than LIB $LiNi_xCo_yMn_zO_2$, and the extent of damage is more severe than those of the LIB $LiNi_xCo_yMn_zO_2$ cathodes possibly due to the large ionic size of the Na.

Indeed, the SEM images of the post-mortem cycled full cell electrodes reveal the efficacy of the AlF_3 coating at a macroscopic scale (Figure 7). The shattered particles are marked by red circles. Even though many of the after-cycled bare NRG65 particles remained intact due to the compact nanorods mechanically strengthening the structural integrity,[37,38] some of the particles still shattered (Figure 7a,b). As demonstrated *via* XRD patterns and TEM images above, electrolyte penetration *via* inter- and intramicrocracks undermines the bulk and surface structure and leads to cathode particle pulverization. Such pulverized active materials become disconnected from the wider electrical network and contribute to accelerated capacity fade. On the other hand, AlF_3−NRG65 particles displayed minimal damage to the overall particle morphology and remained intact as pointed out in Figure 7c,d due to the AlF_3 surface coating obstructing electrolyte penetration, which explains its stable electrochemical performance. A table comparing the electrochemical performance of AlF_3-coated nanorod gradient $Na[Ni_{0.65}Co_{0.13}Mn_{0.27}]O_2$ to other coated layered cathode materials electrochemical performance is shown in Table S2.[30−36,55]

CONCLUSIONS

In summary, we propose an O3-type AlF_3-coated nanorod gradient $Na[Ni_{0.65}Co_{0.08}Mn_{0.27}]O_2$ material as a high-performance cathode active component for SIBs. By combining the nanorod gradient design with an AlF_3 coating, the O3-type AlF_3 coated nanorod gradient $Na[Ni_{0.65}Co_{0.08}Mn_{0.27}]O_2$ cathode material delivers a high discharge capacity (half cell: 160 mAh g^{-1}, full cell: 132 mAh g^{-1} at 0.1 C-rate), high capacity retention (half cell: 89.2%, full cell 96.3% at 0.5 C-rate), and promising rate capability. In addition, we explore the degradation mechanism of Ni-rich $Na[Ni_xCo_yMn_z]O_2$ cathode materials in SIBs. A systematic examination by electrochemical, structural, and optical methods of the post-mortem bare and AlF_3-coated nanorod gradient $Na[Ni_{0.65}Co_{0.08}Mn_{0.27}]O_2$ cathodes clearly demonstrates that an AlF_3 nanolayer coating efficaciously shielded the particle bulk structure from electrolyte infiltration and limited structural degradation to a 4−5 nm thick region on the outer surface, preserving the interior layered structure, even at the particle periphery which is most vulnerable to Na removal. This leads to the preservation of overall particle cohesion and promising electrochemical performance, and we hope that this study will contribute to further development of Ni-rich O3-type $Na[Ni_xCo_yMn_z]O_2$.

METHODS

Synthesis of Nanorod Gradient $Na[Ni_{0.65}Co_{0.08}Mn_{0.27}]O_2$ Cathodes. For the synthesis of the NRG 65, the $[Ni_{0.65}Co_{0.08}Mn_{0.27}](OH)_2$ precursor was prepared as nanorod primary particles *via* co-precipitation,[37,56] in which the chemical-composition gradient varied from the inner end to the outer end. $NiSO_4·6H\ _2O$, $CoSO_4·7H_2O$, and $MnSO_4·H_2O$ were used as starting materials for co-precipitation. Two tanks containing two different solutions were used to control the concentrations of the transition metals. An aqueous solution with a Ni/Co/Mn ion molar ratio of 0.58:0.10:0.32 (tank 2) was slowly pumped into a Ni-rich (molar ratio of Ni/Mn = 0.96:0.04) stock solution (in tank 1). At the initial stage of the co-precipitation process, the Ni-rich aqueous solution (tank 1) was fed first into the 17 L batch reactor filled with a certain amount of deionized water, NH_4OH solution (aq), and NaOH solution (aq). The solution from tank 1 was mixed continuously with the solution from tank 2 (Nideficient solution), and the homogeneously mixed solution was then fed into a batch reactor. Concurrently, a 4.0 mol L^{-1} aqueous NaOH solution and the desired amount of a NH_4OH chelating agent solution (aq) were separately pumped into the reactor. After the composition of tank 1 reached the desired surface composition, feeding from tank 2 was stopped. The concentration of the solution (2 mol L^{-1} for the metal ions), pH (11), temperature (50 °C), and stirring speed of the mixture in the reactor (1000 rpm) were carefully controlled.

Synthesis of Constant Concentration $Na[Ni_{0.65}Co_{0.08}Mn_{0.27}]O_2$ Cathodes. A co-precipitation method[56] was used to synthesize the constant concentration $[Ni_{0.65}Co_{0.08}Mn_{0.27}](OH)_2$ precursors. A homogeneously mixed solution of $NiSO_4{\cdot}6H_2O$, $CoSO_4{\cdot}H_2O$, and $MnSO_4{\cdot}H_2O$ was added into a 17 L batch reactor under a N_2 atmosphere at a reaction temperature of 55 °C. The pH of the solution was kept at 11, and the stirring rate was kept at 550 rpm. The resulting hydroxide precursors from the reactor were filtered, washed, and vacuum dried at 110 °C overnight. The final constant concentration of the $Na[Ni_{0.65}Co_{0.08}Mn_{0.27}]O_2$ cathode was fabricated by mixing the dried hydroxide precursor with NaOH in a 1:1 molar ratio and calcining at 650 °C for 24 h under an oxygen environment and then quenching in vacuum.

Nanosized AlF_3 Particle Synthesis. AlF_3 particles were synthesized as reported previously.[41] In a molar ratio of 1:7, $Al(NO_3)_3{\cdot}9H_2O$ (aq) and NH_4F (aq) were mixed together in a solution. The solution pH was adjusted to 10, and the solvent was evaporated. The obtained $(NH_4)_3AlF_6$ powders were heated at 400 °C for 5 h under N_2 conditions, and the resulting powder was vacuum dried to obtain AlF_3 powders. The resulting AlF_3 particles' SEM image and XRD pattern are shown in Figure S7.

Dry Ball-Mill Coating. To avoid cathode exposure to moisture, the dry ball-mill coating was performed in a dry room. The AlF_3-coated full-concentration gradient $Na[Ni_{0.65}Co_{0.08}Mn_{0.27}]O_2$ was obtained by placing bare $Na[Ni_{0.65}Co_{0.08}Mn_{0.27}]O_2$ and AlF_3 nanoparticles (Sigma-Aldrich, USA) in a polypropylene bottle (Nalgene, USA) with zirconia balls and ball-milling using a ball-mill machine (As One, PM-001, Japan). Coating of the particles was carried out at 100 rpm for 12 h with 1 wt % AlF_3 nanoparticles.

Electrochemical Characterization. The resulting bare and AlF_3-coated sodium metal oxides were mixed with Super-P carbon and polyvinylidene fluoride (PVdF) in a 85:10:5 ratio in *N*-methyl-2-pyrrolidone and cast onto an aluminum foil to achieve active material loading of 2.5−3.0 mg cm^{-2} for half-cells and 5.5−6 mg cm^{-2} for full cells. Afterward, the cast electrodes were vacuum-dried and roll-pressed. Half-cell electrodes were punched out from the electrodes and assembled in 2032 coin-type cells with sodium metal as an anode with 0.5 M $NaPF_6$ in propylene carbonate (PC) + fluoroethylene carbonate (FEC) 2 vol % as electrolyte and cycled from 1.5−4.1 V *versus* Na^0/Na^+ at 0.5C. With Ni-rich O3-type cathodes, it is true that higher capacities could be achieved with an increased cutoff voltage. Due to unwanted side reactions and structural instabilities, the O3-type cathodes are susceptible structural damage, which leads to rapid capacity fading. In the case of SIBs, these problems exacerbate as the stressful monoclinic P′3 to hexagonal P3′′ phase transition occurring above 4.0 V (*vs* Na/Na^+) causes the reversibility of Na ions during charge−discharge to fall significantly. In a previous report,[20] reactive Ni^{4+} in high-Ni cathodes ($x \geq 60$ at%) at a highly charged state (upper cutoff potential of 4.1 V) have been reported to cause partial electrolyte decomposition, leading to substantially poorer capacity retention and rate capability compared to cathodes with low Ni content. Therefore, to achieve reasonable cycling performance along with high capacity, we have decided to cycle between the voltage range of 1.5−4.1 V. Note that 1 C = 150 mA g^{-1}. Pouch-type full cells were fabricated with electrode dimensions of 3 by 5 cm^2 area of both bare and AlF_3 coated nanorod gradient $Na[Ni_{0.65}Co_{0.08}Mn_{0.27}]O_2$ electrodes as the cathode and hard carbon as the anode (active material: PVdF = 8:2). The negative electrode to positive electrode (N/P) capacity ratio of the full cells was 1.15:1, and the fabricated full cells were cycled from 1.0−4.1 V up to 200 cycles at 1C and 25 °C. Electrochemical impedance spectroscopy (EIS) was performed on after-cycled full cells which were charged to 4.1 V with a potentiostat (Bio-Logic, VMP3) from 1 MHz to 1 mHz.

Analytical Techniques. The chemical composition of the prepared precursors and oxides were ascertained by inductively coupled plasma atomic emission spectroscopy (ICP-AES, OPIMA8300, PerkinElmer). Powder X-ray diffraction (XRD, Rigaku, Rint-2000) was performed with Cu Kα radiation at $2\theta = 10{-}80°$ with a step size of 0.01°, and the lattice parameters were obtained from the XRD pattern by Rietveld refinement employing the FullProf software package. Scanning electron microscopy (SEM, JSM-6340F, JEOL) was used to analyze particle before- and after-cycled morphology. Particle cross sections were obtained with a focused-ion beam (FIB), and an electron-probe microanalyzer (EPMA, JXA-8100, JEOL) was used to confirm successful concentration gradient profiles on precursor and sodiated oxides. Transmission electron microscopy (TEM, JEM2010, JEOL) and energy-dispersive X-ray spectroscopy (EDX, JEM 20100F, JEOL) were carried out on the cross-sectioned samples. HF titration was performed with a 5 mL glass buret using a 0.02 N sodium hydroxide (NaOH) aqueous solution. The pH indicator was bromothymol blue (0.04 wt % in water), which appears yellow at pH less than 6 and blue at pH greater than 7. A polypropylene syringe and Erlenmeyer flask were used to prevent possible reaction of glass with HF acid. The titration was performed by placing 3 mL of crushed ice and 1 mL of water in the polypropylene Erlenmeyer flask with a couple drops of bromothymol blue. A 0.2 mL portion of electrolyte was drawn from pristine electrolyte, cycled bare NRG65 pouch cells, and cycled AlF_3−NRG65 pouch cells and weighed and added to the Erlenmeyer flask. The flask was swirled, and NaOH solution was added to the solution until the yellow solution turned blue. If the color returned to yellow after 30 s, more NaOH drops were added. The weight of the empty syringe was taken to determine electrolyte weight, and HF levels were calculated under the assumption that acids were pure HF.

ASSOCIATED CONTENT

Ⓢ Supporting Information

The Supporting Information is available free of charge on the ACS Publications website at DOI: 10.1021/acsnano.8b08266.

> ICP table, NRG65 precursor particle SEM, AlF_3 coated NRG65 particle cross-section and aluminum EDX, CC *vs* bare NRG65 electrochemical data, after-cycled XRD patterns of NRG65 and AlF_3−NRG65 half-cell XRD patterns, and EIS measurement scheme (PDF)

AUTHOR INFORMATION

Corresponding Authors

*E-mail: mullins@che.utexas.edu.
*E-mail: csyoon@hanyang.ac.kr.

ORCID

Chong Seung Yoon: 0000-0001-6164-3331
Adam Heller: 0000-0003-0181-1246
C. Buddie Mullins: 0000-0003-1030-4801

Notes

The authors declare no competing financial interest.

ACKNOWLEDGMENTS

The authors gratefully acknowledge support from the Welch Foundation *via* Grant Nos. F-1131 (A.H.) and F-1436 (C.B.M.) and also the National Science Foundation through Grant No. CBET-1603491. The authors also thank Y.-K. Sun at Hanyang University for providing the hydroxide precursors for the NRG65 samples.

REFERENCES

(1) Scrosati, B.; Hassoun, J.; Sun, Y.-K. Lithium-Ion Batteries. A Look into the Future. *Energy Environ. Sci.* **2011**, *4*, 3287.

(2) Etacheri, V.; Marom, R.; Elazari, R.; Salitra, G.; Aurbach, D. Challenges in the Development of Advanced Li-Ion Batteries: A Review. *Energy Environ. Sci.* **2011**, *4*, 3243−3262.

(3) Palacín, M. R.; De Guibert, A. Batteries: Why Do Batteries Fail? *Science* **2016**, *351* (6273), 1253292.

(4) Forster, J.; Rutherford, T. F. *A Lithium Shortage: Are Electric Vehicles Under Threat?* ETH, 2011.

(5) Perkel, J. M. The Trouble with Lithium Implications of Future PHEV Production for Lithium Demand. *Nature* **2015**, *521*, 111−112.

(6) Slater, M. D.; Kim, D.; Lee, E.; Johnson, C. S. Sodium-Ion Batteries. *Adv. Funct. Mater.* **2013**, *23*, 947−958.

(7) Hwang, J.-Y.; Myung, S.-T.; Sun, Y.-K. Sodium-Ion Batteries: Present and Future. *Chem. Soc. Rev.* **2017**, *46*, 3529−3614.

(8) Oh, S. M.; Myung, S. T.; Hassoun, J.; Scrosati, B.; Sun, Y.-K. Reversible $NaFePO_4$ Electrode for Sodium Secondary Batteries. *Electrochem. Commun.* **2012**, *22*, 149−152.

(9) Chihara, K.; Kitajou, A.; Gocheva, I. D.; Okada, S.; Yamaki, J. I. Cathode Properties of $Na_3M_2(PO_4)_2F_3$ [M = Ti, Fe, V] for Sodium-Ion Batteries. *J. Power Sources* **2013**, *227*, 80−85.

(10) Ratnakumar, B. V.; Di Stefano, S.; Williams, R. M.; Nagasubramanian, G.; Bankston, C. P. Organic Cathode Materials in Sodium Batteries. *J. Appl. Electrochem.* **1990**, *20*, 357−364.

(11) Yabuuchi, N.; Kajiyama, M.; Iwatate, J.; Nishikawa, H.; Hitomi, S.; Okuyama, R.; Usui, R.; Yamada, Y.; Komaba, S. P2-Type $Na_x[Fe_{1/2}Mn_{1/2}]O_2$ made from Earth-Abundant Elements for Rechargeable Na Batteries. *Nat. Mater.* **2012**, *11*, 512−517.

(12) Berthelot, R.; Carlier, D.; Delmas, C. Electrochemical Investigation of the P2−Na_xCoO_2 Phase Diagram. *Nat. Mater.* **2011**, *10*, 74−80.

(13) Buchholz, D.; Chagas, L. G.; Winter, M.; Passerini, S. P2-Type Layered $Na_{0.45}Ni_{0.22}Co_{0.11}Mn_{0.66}O_2$ as Intercalation Host Material for Lithium and Sodium Batteries. *Electrochim. Acta* **2013**, *110*, 208−213.

(14) D'Arienzo, M.; Ruffo, R.; Scotti, R.; Morazzoni, F.; Mari, C. M.; Polizzi, S. Layered $Na_{0.71}CoO_2$: A Powerful Candidate for Viable and High Performance Na-Batteries. *Phys. Chem. Chem. Phys.* **2012**, *14*, 5945−5952.

(15) Yu, T.-Y.; Hwang, J.-Y.; Aurbach, D.; Sun, Y.-K. Microsphere $Na_{0.65}[Ni_{0.17}Co_{0.11}Mn_{0.72}]O_2$ Cathode Material for High-Performance Sodium-Ion Batteries. *ACS Appl. Mater. Interfaces* **2017**, *9*, 44534−44541.

(16) Yabuuchi, N.; Yano, M.; Yoshida, H.; Kuze, S.; Komaba, S. Synthesis and Electrode Performance of O3-Type $NaFeO_2$-$NaNi_{1/2}Mn_{1/2}O_2$ Solid Solution for Rechargeable Sodium Batteries. *J. Electrochem. Soc.* **2013**, *160*, A3131−A3137.

(17) Xia, X.; Dahn, J. R. $NaCrO_2$ is a Fundamentally Safe Positive Electrode Material for Sodium-Ion Batteries with Liquid Electrolytes. *Electrochem. Solid-State Lett.* **2012**, *15*, A1−A4.

(18) Oh, S. M.; Myung, S. T.; Jang, M. W.; Scrosati, B.; Hassoun, J.; Sun, Y.-K. An Advanced Sodium-Ion Rechargeable Battery Based on a Tin-Carbon Anode and a Layered Oxide Framework Cathode. *Phys. Chem. Chem. Phys.* **2013**, *15*, 3827−3833.

(19) Oh, S.-M.; Myung, S.-T.; Yoon, C. S.; Lu, J.; Hassoun, J.; Scrosati, B.; Amine, K.; Sun, Y.-K. Advanced $Na[Ni_{0.25}Fe_{0.5}Mn_{0.25}]O_2$/C−$Fe_3O_4$ Sodium-Ion Batteries Using EMS Electrolyte for Energy Storage. *Nano Lett.* **2014**, *14*, 1620−1626.

(20) Hwang, J.-Y.; Yoon, C. S.; Belharouak, I.; Sun, Y.-K. A Comprehensive Study of the Role of Transition Metals in O3-Type Layered $Na[Ni_xCo_yMn_z]O_2$ (x = 1/3, 0.5, 0.6, and 0.8) Cathodes for Sodium-Ion Batteries. *J. Mater. Chem. A* **2016**, *4*, 17952−17959.

(21) Guo, S.; Yu, H.; Liu, P.; Ren, Y.; Zhang, T.; Chen, M.; Ishida, M.; Zhou, H. High-Performance Symmetric Sodium-Ion Batteries Using a New, Bipolar O3-Type Material, $Na_{0.8}Ni_{0.4}Ti_{0.6}O_2$. *Energy Environ. Sci.* **2015**, *8*, 1237−1244.

(22) Komaba, S.; Yabuuchi, N.; Nakayama, T.; Ogata, A.; Ishikawa, T.; Nakai, I. Study on the Reversible Electrode Reaction of $Na_{1-X}Ni_{0.5}Mn_{0.5}O_2$ for a Rechargeable Sodium-Ion Battery. *Inorg. Chem.* **2012**, *51*, 6211−6220.

(23) Bo, S. H.; Li, X.; Toumar, A. J.; Ceder, G. Layered-to-Rock-Salt Transformation in Desodiated Na_xCrO_2 (x = 0.4). *Chem. Mater.* **2016**, *28*, 1419−1429.

(24) Yabuuchi, N.; Kubota, K.; Dahbi, M.; Komaba, S. Research Development on Sodium-Ion Batteries. *Chem. Rev.* **2014**, *114*, 11636−11682.

(25) Yabuuchi, N.; Kawamoto, Y.; Hara, R.; Ishigaki, T.; Hoshikawa, A.; Yonemura, M.; Kamiyama, T.; Komaba, S. A Comparative Study of $LiCoO_2$ Polymorphs: Structural and Electrochemical Characterization of O2-, O3-, and O4-Type Phases. *Inorg. Chem.* **2013**, *52*, 9131−9142.

(26) Liu, L.; Wang, Z.; Li, H.; Chen, L.; Huang, X. Al_2O_3-Coated $LiCoO_2$ as Cathode Material for Lithium Ion Batteries. *Solid State Ionics* **2002**, *152−153*, 341−346.

(27) Chen, Z.; Qin, Y.; Amine, K.; Sun, Y.-K. Role of Surface Coating on Cathode Materials for Lithium-Ion Batteries. *J. Mater. Chem.* **2010**, *20*, 7606−7612.

(28) Appapillai, A. T.; Mansour, A. N.; Cho, J.; Shao-Horn, Y. Microstructure of $LiCoO_2$ with and without "$AlPO_4$" Nanoparticle Coating: Combined STEM and XPS Studies. *Chem. Mater.* **2007**, *19*, 5748−5757.

(29) Sun, Y.-K.; Yoon, C. S.; Myung, S.-T.; Belharouak, I.; Amine, K. Role of AlF_3 Coating on $LiCoO_2$ Particles during Cycling to Cutoff Voltage above 4.5 V. *J. Electrochem. Soc.* **2009**, *156*, A1005−A1010.

(30) Jo, J. H.; Choi, J. U.; Konarov, A.; Yashiro, H.; Yuan, S.; Shi, L.; Sun, Y.-K.; Myung, S. T. Sodium-Ion Batteries: Building Effective Layered Cathode Materials with Long-Term Cycling by Modifying the Surface *via* Sodium Phosphate. *Adv. Funct. Mater.* **2018**, *28*, 1−11.

(31) Yang, S. J.; Kang, J. H.; Jung, H.; Kim, T.; Park, C. R. Simultaneous MgO Coating and Mg Doping of Na[Ni0.5Mn0.5]O2 Cathode: Facile and Customizable Approach to High-Voltage Sodium-Ion Batteries. *J. Mater. Chem. A* **2013**, *1*, 9427−9432.

(32) Ramasamy, H. V.; Kaliyappan, K.; Thangavel, R.; Aravindan, V.; Kang, K.; Kim, D. U.; Park, Y.; Sun, X.; Lee, Y. S. Cu-Doped P2-$Na_{0.5}Ni_{0.33}Mn_{0.67}O_2$ encapsulated with MgO as a Novel High Voltage Cathode with Enhanced Na-Storage Properties. *J. Mater. Chem. A* **2017**, *5*, 8408−8415.

(33) Kaliyappan, K.; Liu, J.; Xiao, B.; Lushington, A.; Li, R.; Sham, T.-K.; Sun, X. Enhanced Performance of P2-$Na_{0.66}(Mn_{0.54}Co_{0.13}Ni_{0.13})O_2$ Cathode for Sodium-Ion Batteries by Ultrathin Metal Oxide Coatings *via* Atomic Layer Deposition. *Adv. Funct. Mater.* **2017**, *27*, 1701870.

(34) Kaliyappan, K.; Liu, J.; Lushington, A.; Li, R.; Sun, X. Highly Stable $Na_{2/3}(Mn_{0.54}Ni_{0.13}Co_{0.13})O_2$ Cathode Modified by Atomic Layer Deposition for Sodium-Ion Batteries. *ChemSusChem* **2015**, *8*, 2537−2543.

(35) Liu, Y.; Fang, X.; Zhang, A.; Shen, C.; Liu, Q.; Enaya, H. A.; Zhou, C. Layered P2-$Na_{2/3}[Ni_{1/3}Mn_{2/3}]O_2$ as High-Voltage Cathode for Sodium-Ion Batteries: The Capacity Decay Mechanism and Al2O3surface Modification. *Nano Energy* **2016**, *27*, 27−34.

(36) Hwang, J. Y.; Myung, S. T.; Choi, J. U.; Yoon, C. S.; Yashiro, H.; Sun, Y.-K. Resolving the Degradation Pathways of the O3-Type Layered Oxide Cathode Surface through the Nano-Scale Aluminum Oxide Coating for High-Energy Density Sodium-Ion Batteries. *J. Mater. Chem. A* **2017**, *5*, 23671−23680.

(37) Hwang, J. Y.; Oh, S. M.; Myung, S. T.; Chung, K. Y.; Belharouak, I.; Sun, Y.-K. Radially Aligned Hierarchical Columnar Structure as a Cathode Material for High Energy Density Sodium-Ion Batteries. *Nat. Commun.* **2015**, *6*, 1−9.

(38) Hwang, J. Y.; Myung, S. T.; Yoon, C. S.; Kim, S. S.; Aurbach, D.; Sun, Y.-K. Novel Cathode Materials for Na-Ion Batteries Composed of Spoke-Like Nanorods of $Na[Ni_{0.61}Co_{0.12}Mn_{0.27}]O_2$ Assembled in Spherical Secondary Particles. *Adv. Funct. Mater.* **2016**, *26*, 8083−8093.

(39) Sun, Y.-K.; Lee, M. J.; Yoon, C. S.; Hassoun, J.; Amine, K.; Scrosati, B. The Role of AlF_3 Coatings in Improving Electrochemical

Cycling of Li-Enriched Nickel-Manganese Oxide Electrodes for Li-Ion Batteries. *Adv. Mater.* **2012**, *24*, 1192−1196.

(40) Xie, J.; Sendek, A. D.; Cubuk, E. D.; Zhang, X.; Lu, Z.; Gong, Y.; Wu, T.; Shi, F.; Liu, W.; Reed, E. J.; Cui, Yi Atomic Layer Deposition of Stable $LiAlF_4$ Lithium Ion Conductive Interfacial Layer for Stable Cathode Cycling. *ACS Nano* **2017**, *11*, 7019−7027.

(41) Lee, S. H.; Yoon, C. S.; Amine, K.; Sun, Y.-K. Improvement of Long-Term Cycling Performance of $Li[Ni_{0.8}Co_{0.15}Al_{0.05}]O_2$ by AlF3coating. *J. Power Sources* **2013**, *234*, 201−207.

(42) Zheng, J.; Gu, M.; Xiao, J.; Polzin, B. J.; Yan, P.; Chen, X.; Wang, C.; Zhang, J. G. Functioning Mechanism of AlF_3 Coating on the Li- and Mn-Rich Cathode Materials. *Chem. Mater.* **2014**, *26*, 6320−6327.

(43) Rodríguez-Carvajal; FULLPROF, J. A Program for Rietveld Refinement and Pattern Matching Analysis. *Abstr. Satell. Meet. Powder Diffr. XV Congr. IUCr* **1990**, 127.

(44) Delmas, C.; Fouassier, C.; Hagenmuller, P. Structural Classification and Properties of the Layered Oxides. *Physica B+C* **1980**, *99*, 81−85.

(45) Sun, Y.-K.; Myung, S. T.; Park, B. C.; Prakash, J.; Belharouak, I.; Amine, K. High-Energy Cathode Material for Long-Life and Safe Lithium Batteries. *Nat. Mater.* **2009**, *8*, 320−324.

(46) Sun, Y.-K.; Chen, Z.; Noh, H. J.; Lee, D. J.; Jung, H. G.; Ren, Y.; Wang, S.; Yoon, C. S.; Myung, S. T.; Amine, K. Nanostructured High-Energy Cathode Materials for Advanced Lithium Batteries. *Nat. Mater.* **2012**, *11*, 942−947.

(47) Kim, U. H.; Lee, E. J.; Yoon, C. S.; Myung, S. T.; Sun, Y.-K. Compositionally Graded Cathode Material with Long-Term Cycling Stability for Electric Vehicles Application. *Adv. Energy Mater.* **2016**, *6*, 1−8.

(48) Delmas, C.; Saadoune, I. Electrochemical and Physical Properties of the $Li_xNi_{1-y}Co_yO_2$ Phases. *Solid State Ionics* **1992**, *53*−*56*, 370−375.

(49) Vijayakumar, R.; Shivaramu; Rajasekaran, L.; Ramamurthy, N.; Ford, M. J. Compton Profile of Polycrystalline Sodium Chloride and Sodium Fluoride. *Nucl. Instrum. Methods Phys. Res., Sect. B* **2005**, *234*, 185−193.

(50) Jacoboni, C.; Leble, A.; Rousseau, J. J. Détermination Précise de La Structure de La Chiolite $Na_5Al_3F_{14}$ Etétude Par R.P.E. de $Na_5Al_3F_{14}$:Cr^3+. *J. Solid State Chem.* **1981**, *36*, 297−304.

(51) Kozen, A. C.; Pearse, A. J.; Lin, C.-F.; Noked, M.; Rubloff, G. W. Atomic Layer Deposition of the Solid Electrolyte LiPON. *Chem. Mater.* **2015**, *27*, 5324−5331.

(52) Cao, H.; Xia, B.; Zhang, Y.; Xu, N. $LiAlO_2$-Coated $LiCoO_2$ as Cathode Material for Lithium Ion Batteries. *Solid State Ionics* **2005**, *176*, 911−914.

(53) Ryu, H. H.; Park, K. J.; Yoon, C. S.; Sun, Y.-K. Capacity Fading of Ni-Rich $Li[Ni_xCo_yMn_{1-x-y}]O_2$ ($0.6 \leq x \leq 0.95$) Cathodes for High-Energy-Density Lithium-Ion Batteries: Bulk or Surface Degradation? *Chem. Mater.* **2018**, *30*, 1155−1163.

(54) Yoon, C. S.; Jun, D.-W.; Myung, S.-T.; Sun, Y.-K. Structural Stability of $LiNiO_2$ Cycled above 4.2 V. *ACS Energy Lett.* **2017**, *2*, 1150−1155.

(55) Ding, J. J.; Zhou, Y. N.; Sun, Q.; Fu, Z. W. Cycle Performance Improvement of $NaCrO_2$ Cathode by Carbon Coating for Sodium Ion Batteries. *Electrochem. Commun.* **2012**, *22*, 85−88.

(56) Lee, M. H.; Kang, Y. J.; Myung, S. T.; Sun, Y.-K. Synthetic Optimization of $Li[Ni_{1/3}Co_{1/3}Mn_{1/3}]O_2$ *via* Co-Precipitation. *Electrochim. Acta* **2004**, *50*, 939−948.